Bioactive Materials 41 (2024) 611–626

Contents lists available at ScienceDirect

Bioactive Materials

journal homepage: www.keaipublishing.com/en/journals/bioactive-materials

# Framework nucleic Acid-MicroRNA mediated hepatic differentiation and functional hepatic spheroid development for treating acute liver failure

Hongyan Wei [a,b,c,d,1], Tiantian Xue [a,1], Fenfang Li [a], Enguo Ju [a], Haixia Wang [a], Mingqiang Li [a,b], Yu Tao [a,b,*]

[a] Laboratory of Biomaterials and Translational Medicine, Center for Nanomedicine, The Third Affiliated Hospital, Sun Yat-sen University, Guangzhou, 510630, Guangdong, China
[b] Guangdong Provincial Key Laboratory of Liver Disease Research, Sun Yat-sen University, Guangzhou, 510630, Guangdong, China
[c] Department of Obstetrics and Gynecology, Women and Children's Hospital of Chongqing Medical University, No.120 Longshan Road, Yubei District, Chongqing, 401147, China
[d] Department of Obstetrics and Gynecology, Chongqing Health Center for Women and Children, No.120 Longshan Road, Yubei District, Chongqing, 401147, China

ARTICLE INFO

*Keywords:*
Hepatic differentiation
Framework nucleic acid
Functional hepatic spheroids
Transcriptome sequencing analysis
Acute liver failure therapy

ABSTRACT

The specific induction of hepatic differentiation presents a significant challenge in developing alternative liver cell sources and viable strategies for clinical therapy of acute liver failure (ALF). The past decade has witnessed the blossom of microRNAs in regenerative medicine. Herein, microRNA 122-functionalized tetrahedral framework nucleic acid (FNA-miR-122) has emerged as an unprecedented and potential platform for directing the hepatic differentiation of adipose-derived mesenchymal stem cells (ADMSCs), which offers a straightforward and cost-effective method for generating functional hepatocyte-like cells (FNA-miR-122-iHep). Additionally, we have successfully established a liver organoid synthesis strategy by optimizing the co-culture of FNA-miR-122-iHep with endothelial cells (HUVECs), resulting in functional Hep:HUE-liver spheroids. Transcriptome analysis not only uncovered the potential molecular mechanisms through which miR-122 influences hepatic differentiation in ADMSCs, but also clarified that Hep:HUE-liver spheroids could further facilitate hepatocyte maturation and improved tissue-specific functions, which may provide new hints to be used to develop a hepatic organoid platform. Notably, compared to transplanted ADMSCs and Hep-liver spheroid, respectively, both FNA-miR-122-iHep-based single cell therapy and Hep:HUE-liver spheroid-based therapy showed high efficacy in treating ALF in vivo. Collectively, this research establishes a robust system using microRNA to induce ADMSCs into functional hepatocyte-like cells and to generate hepatic organoids in vitro, promising a highly efficient therapeutic approach for ALF.

## 1. Introduction

Despite progress in cell reprogramming using transcription factors that enable the conversion of somatic cells [1] and stem cells [2] into hepatocytes, clinical applications of this technology remain limited by several deficiencies, including the use of viral DNA delivery vectors [3] and the overexpression of exogenous transcription factor [4]. Consequently, there is a pressing need for new methods that ensure secure and efficient hepatocyte production. Previous research has highlighted microRNAs (miRNAs) as promising candidates for cell reprogramming. MiRNAs have significantly advanced the self-renewal and differentiation of stem cells [5] by forming intricate regulatory networks and modulating gene expression at post-transcriptional levels through interactions with mRNAs [6]. It has been proven that 50% of human protein-coding genes are regulated by miRNA [7]. These transient, endogenous, single-stranded, non-encoding RNAs bind partially or completely to mRNA sequences, inducing target gene silencing without integrating into the host genome [8], thereby influencing various cellular functions and physiological processes [9]. To date, over one thousand miRNAs have been identified as regulators of key biological

Peer review under responsibility of KeAi Communications Co., Ltd.
* Corresponding author. Laboratory of Biomaterials and Translational Medicine, Center for Nanomedicine, The Third Affiliated Hospital, Sun Yat-sen University, Guangzhou, 510630, Guangdong, China.
*E-mail address:* taoy28@mail.sysu.edu.cn (Y. Tao).
[1] These authors contributed equally to this work.

https://doi.org/10.1016/j.bioactmat.2024.08.022
Received 5 May 2024; Received in revised form 6 August 2024; Accepted 20 August 2024

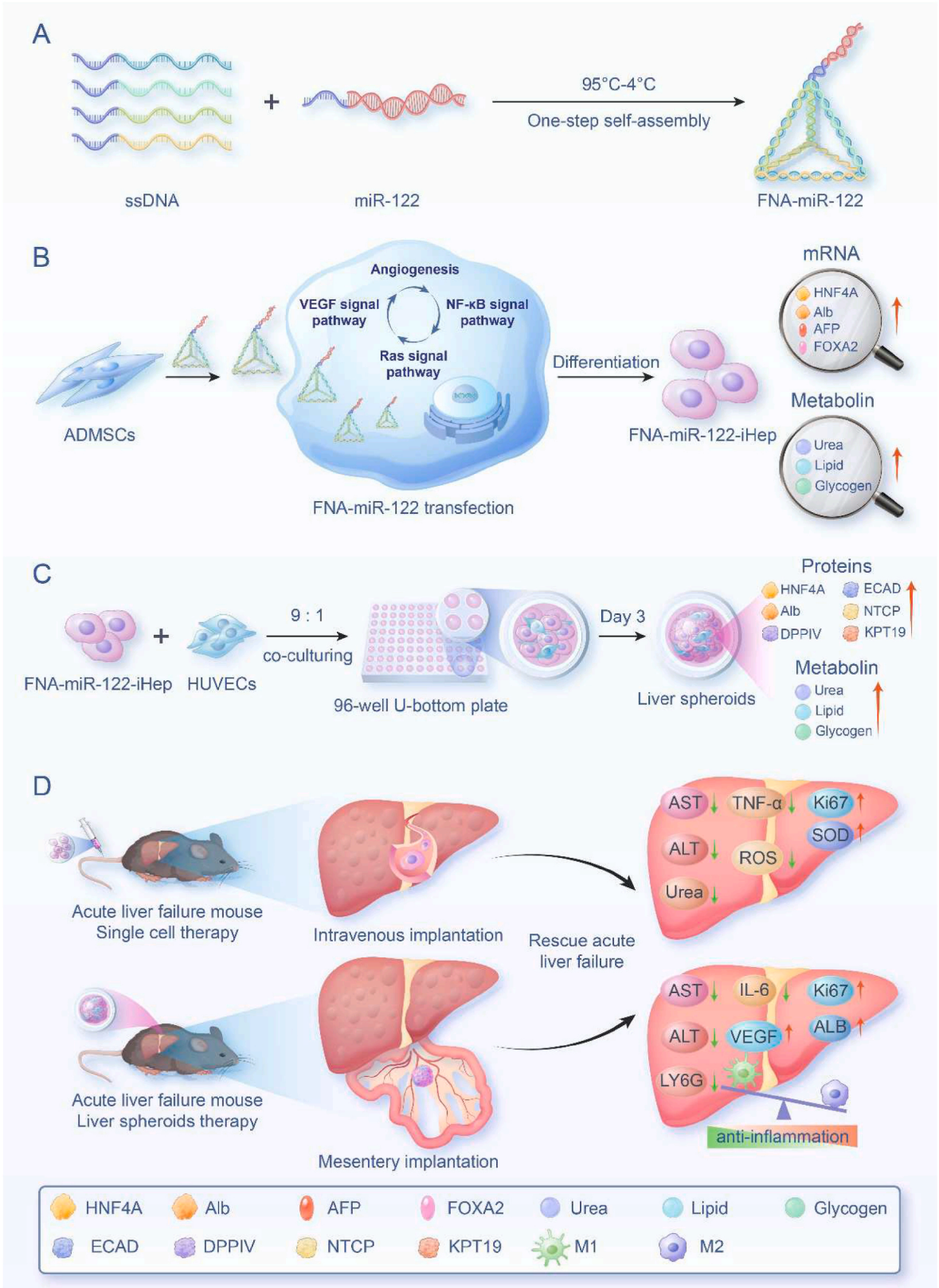


**Scheme 1.** Schematic illustration displaying that FNA-miR-122 promoted hepatic differentiation, and facilitated the generation of the FNA-miR-122-iHep-based liver spheroids. The diagram highlighted that two modes of transplantations achieved highly efficient ALF therapy in vivo.

processes, including differentiation, proliferation, apoptosis, and aging [10]. Moreover, growing evidence has demonstrated that targeted manipulation of miRNAs, either by overexpression or knockout, can directionally regulate the hepatic differentiation of stem cells, offering substantial potential in regenerative medicine [11]. MicroRNA 122 (miR-122), in particular, has been recognized as a significant regulator during hepatogenesis, promoting the hepatic differentiation of liver progenitor cells [12]. Accordingly, accumulating evidence has verified that miR-122 was an important regulator of human stem cell differentiation into hepatocytes [13,14]. However, whether miR-122 can promote hepatic differentiation of stem cells in the absence of cytokines, growth factors and other external factors needs to be further investigated.

Adipose-derived mesenchymal stem cells (ADMSCs), recognized for their multipotency, self-renewal capacity, and non-invasive accessibility [15,16], hold substantial potential for hepatic-specific differentiation [17]. The process of differentiating human ADMSCs (hADMSCs) into hepatocyte-like cells (iHeps) is complex [18], influenced by multiple genes, and remains dynamic and interdependent [19]. Particularly, the role of miRNAs in this process is still not well understood, highlighting a critical area for research to enhance the efficiency of hepatic differentiation. Moreover, to simulate the liver's microenvironment and improve hepatocyte function, co-culturing experiments have been conducted with various liver and non-liver cell types, including umbilical vein endothelial cells [20], sinusoidal endothelial cells [21], fibroblasts [22], mesenchymal stem cells [23], Kupffer cells [24], and stellate cells [25], to generate liver spheroids or microlivers [26]. Primary hepatocytes often dedifferentiate and lose functionality when isolated and cultured [27]. Moreover, obtaining a sufficient number of functional primary hepatocytes remains a significant bottleneck. To address these challenges, three-dimensional (3D) spheroid and organoid therapies using iHeps have been developed [28]. These therapies offer advantages over traditional liver transplantation, including minimal invasiveness, potential for reuse, and avoidance of chronic immunosuppression [29], thus presenting a promising alternative for treating severe hepatic diseases. As a novel supporting cell source, human umbilical vein endothelial cells (HUVECs) have proven effective as co-culture partners with hepatocytes, which replicates the in vivo physiology structure where hepatocytes and HUVECs constitute the continuous lining along the sinusoid separated by the Disse space [30]. HUVECs facilitate vascularization, improving oxygen supply, nutrient delivery, and genetic stability of the cells within the bioengineered constructs [31]. Thus, the integration of iHeps with HUVECs to form composite liver spheroids represents a significant advancement in developing effective therapies for liver diseases.

The transfer of functional miR-122 to stem cells holds potential as an alternative and reproducible source of primary cells for direct hepatic differentiation. Although promising, the inherent instability of the single-stranded miR-122 and its hydrophilic nature, coupled with the barrier of the cell's plasma membrane, present significant challenges for effective delivery [32]. One potential solution is the designing of the double-stranded miR-122 that comprises a guide strand and a sticky-end bearing passenger strand, which may overcome the relative instability of single-stranded RNA [6]. Nonetheless, it remains unclear whether non-viral nanovector-mediated miR-122 delivery could promote the differentiation of ADMSCs into iHep and rescue carbon tetrachloride ($CCl_4$) induced acute liver failure (ALF), which has high morbidity and mortality worldwide. Recent advancements in tetrahedral framework nucleic acid nanorobotics (FNA), which are DNA frameworks built only by oligonucleotides, have garnered significant interest as a natural vector for miRNA transfer [33]. These structures offer notable benefits, including intrinsic biocompatibility, low immunogenicity, excellent biostability, biodegradability, and high drug-loading capacity [34–38]. Furthermore, compared to liposomes or biodegradable polymers, the amounts and locations of nucleic acid cargos in the delivery systems of FNA nanostructures can be easily and precisely regulated. We hypothesize that loading miR-122 onto FNA (FNA-miR-122) could address its stability issues and enhance the hepatic differentiation efficiency of ADMSCs. This approach might provide a simpler and more cost-effective alternative to using growth factors for inducing ADMSCs into functional iHeps [12], thus supporting the development of innovative therapies for ALF [39,40].

Herein, we established an efficient gene delivery platform (FNA-miR-122), which was self-assembled by mixing stoichiometric quantities of strands $T_1$-$T_4$ with miR-122, allowing miR-122 to hybridize with the single-stranded protruding sequence of FNA (Scheme 1). On one hand, FNA-miR-122 facilitated the specific induction of hepatic differentiation in ADMSCs without the need for cytokine cocktails. Transcriptome analysis has elucidated the potential molecular mechanisms by which FNA-miR-122 promotes hepatic differentiation. On the other hand, the hepatic spheroids created by mixing FNA-miR-122-iHep and HUVECs at an optimal ratio of 9:1 exhibited high hepatocyte functions. Of note, the regulation of signal transduction networks also revealed through transcriptomics, aligns with the stages of hepatic differentiation of ADMSCs and hepatocyte regeneration, thereby improving the effectiveness of functional recovery and injury repair in ALF treatment. Additionally, transplantation of FNA-miR-122-iHep and FNA-miR-122-iHep-based liver spheroids based on this platform demonstrated significant therapeutic effects in the mouse ALF model. We anticipate that this FNA-miR-122-mediated differentiation method will facilitate the straightforward production of iHep and liver spheroids, offering a promising approach for ALF therapy.

## 2. Materials and methods

### 2.1. Preparation of FNA-miR-122 via a one-step self-assembly procedure

In brief, four types of pre-designed single-stranded DNAs (ssDNAs) (T1, T2, T3, T4) and miR-122 (see Table S1 for detailed sequences) were mixed in equimolar concentrations in a Tris-magnesium sulfate buffer (5 mM $MgCl_2$, 10 mM Tris-HCl, pH 8.0, Beyotime, China). The mixture was heated at 95 °C for 5 min and then allowed to cool gradually to room temperature. The formation of the FNA-miR-122 complex was confirmed using 2 % agarose gel electrophoresis stained with ethidium bromide (0.5 μg/mL, Sigma-Aldrich, USA), run at 100 V for 30 min, and visualized under UV light at 312 nm. Atomic force microscopy (AFM, Nanoscope V Dimension Icon, Bruker AXS, US) and dynamic light scattering (DLS, Malvern Zetasizer Nano ZS, UK) were employed to characterize the morphology, size, and zeta potential of the FNA-miR-122 complex.

### 2.2. Intracellular uptake of FNA-miR-122

The human adipose tissue-derived mesenchymal stem cells (hADMSCs) were cultured in 6-well plates to approximately 90% confluence. Prior to the experiments, cells were washed three times with phosphate-buffered saline (PBS) and then incubated with a medium containing fluorescein (FAM)-labeled FNA and FAM-labeled FNA-miR-122 for 2 h. Post-incubation, cells were centrifuged at 1000 rpm for 5 min, washed twice with PBS, and the intracellular fluorescence was quantified using a flow cytometer (NovoCyte, Santiago, California, USA).

### 2.3. Subcellular locations and endocytosis mechanism

A colocalization assay was used to study the intracellular trafficking and localization of FNA-miR-122 inside living cells. The hADMSCs were seeded in a 35 mm confocal dish (coverglass-bottom dish) (MatTek Corp, Ashland, MA, USA) at a density of $1 \times 10^4$ cells/cm$^2$ under standard culture conditions. Then, the cells were washed twice with PBS, and incubated with FAM-labeled FNA-miR-122 for 6 and 12 h. Next, the cells were washed by PBS 3 times and stained with 10 μM LysoTracker

Red for 30 min and Hoechst 33342 for 15 min, respectively. Finally, the cells were washed with PBS buffer 3 times before being observed with a confocal laser scanning microscope (FV1000, Olympus, Tokyo, Japan). The excitation wavelengths were set at 405 nm and 543 nm, and the corresponding emission wavelengths were in the range of 430/480 nm and 550/630 nm for Hoechst 33342 and FAM, respectively.

To investigate the endocytosis mechanism, cells ($1 \times 10^5$) were pre-incubated with endocytosis inhibitors such as chlorpromazine (CPZ, 10 μM) or ethylisopropylamiloride (EIPA, 50 μM) before the addition of FAM-labeled-FNA-miR-122. After 30 min, FAM-labeled-FNA-miR-122 (200 nM) was added to each sample in serum-free media and incubated for an additional 6 h at 37 °C in a $CO_2$ incubator. Post-incubation, cells were harvested, washed twice with 1 mL of PBS, and resuspended in 500 μL of ice-cold PBS. Internalization of FNA-miR-122 was quantified using a flow cytometer (Beckman, CytoFLEX, USA). For each sample, 10000 events were recorded in triplicates and the levels of internalization were reported as mean ± standard deviation (SD).

### 2.4. Hepatic differentiation and characterization

hADMSCs were cultured in a serum-free special medium (Saliai Stem Cell Science and Technology Co., LTD, Guangzhou, China) under a humidified atmosphere of 5 % $CO_2$ at 37 °C. Cells were seeded at a density of $2 \times 10^5$ cells/mL in 24-well plates and treated with 200 nM FNA-miR-122. The medium was refreshed every 2 days for continuous cultivation for 21 days. Hepatic differentiation was evaluated by morphological changes and functional assays. Quantitative real-time polymerase chain reaction (qRT-PCR) and transcriptome analysis assessed the expression of hepatocyte markers including hepatocyte nuclear factor 4 alpha (HNF4A), albumin (ALB), E-cadherin (ECAD), alpha-fetoprotein (AFP), and forkhead box A2 (FOXA2). Immunofluorescent staining confirmed the presence of ALB, ECAD, and HNF4A proteins, along with the accumulation of glycogen and lipids, consistent with mature hepatocyte functionality.

### 2.5. qRT-PCR for mRNA quantification

Cells were planted on 6-well culture plates at a density of $1 \times 10^6$ cells/well. The total RNA was extracted from various cell types using RNA-Solv reagent according to the manufacturer's instructions. The standard HiScript II One Step qRT-PCR SYBR® Green Kit protocol was used to carry out the qRT-PCR experiments. The housekeeping gene beta-actin (β-actin) was used for standardization, which was conducted in quadruplicate. The quality and quantity of RNA were verified via agarose gel electrophoresis and measurement with a NanoDrop ND-2000 spectrophotometer (NanoDrop, Wilmington, DE, USA). The expression of β-actin was used to standardize the relative mRNA fold change. The qRT-PCR primer sequences are detailed in Table S2.

### 2.6. Immunofluorescent staining

Cells were fixed at room temperature using 4% paraformaldehyde (PFA) for 20 min. After centrifugation for 5 min, the PFA was discarded. The cells were re-suspended in 0.2 % Triton X-100 for 10 min. The cells were then blocked with goat serum for 30 min before staining with antibodies. After being washed with PBS, the cells were incubated with the monoclonal antibodies against ECAD (1:1000, Cell Signaling), ALB (1:1000, Invitrogen), and HNF4A (1:50, Cell Signaling) at 4 °C overnight. Next, the cells were washed twice with PBS, and Alexa 488-labeled goat anti-rabbit secondary antibody (1:500, Invitrogen) was applied for 2 h. After washing with PBS, the cells were stained with nuclear dye DAPI for 5 min at room temperature and analyzed using confocal microscopy.

### 2.7. Oil Red-O staining and Periodic acid-schiff

Oil Red-O (ORO) (Solarbio) staining and Periodic acid-Schiff (PAS) (Servicebio) were performed following the manufacturer's instructions.

### 2.8. RNA extraction and library construction

Total RNA was extracted using TRIzol reagent (Invitrogen, Carlsbad, CA, USA) according to the manufacturer's instructions. The quantity and purity of RNA from each sample were measured using a NanoDrop ND-1000 spectrophotometer (NanoDrop, Wilmington, DE, USA). The RNA integrity was assessed with an RNA Integrity Number (RIN) greater than 7.0, using a Bioanalyzer 2100 (Agilent, CA, USA), and confirmed by denaturing agarose gel electrophoresis. Poly(A) RNA was purified from 1 μg of total RNA using Dynabeads Oligo(dT) (Thermo Fisher, CA, USA), followed by two rounds of purification. The RNA was then fragmented into small pieces using a Magnesium RNA Fragmentation Module (NEB, cat. e6150, USA) at 94 °C for 5–7 min. Fragmented RNA was reverse transcribed into cDNA using SuperScript™ II Reverse Transcriptase (Invitrogen, cat. 1896649, USA), which was next used to synthesize U-labeled second-stranded DNAs with *E. coli* DNA polymerase I (NEB, cat. m0209, USA), RNase H (NEB, cat.m0297, USA) and dUTP Solution (Thermo Fisher, cat. R0133, USA). An A-base was added to the blunt ends of each strand for adapter ligation, with each adapter containing a T-base overhang. Adapters were ligated to the A-tailed fragments, and size selection was performed using AMPureXP beads. U-labeled second-stranded DNAs were treated with heat-labile UDG enzyme (NEB, cat. m0280, USA), and PCR amplification followed: initial denaturation at 95 °C for 3 min, 8 cycles of denaturation at 98 °C for 15 s, annealing at 60 °C for 15 s, and extension at 72 °C for 30 s, with a final extension at 72 °C for 5 min. The average insert size of the final cDNA library was 300 ± 50 bp. Sequencing was performed using 2 × 150 bp paired-end sequencing (PE150) on an Illumina NovaSeq™ 6000 (LC-Bio Technology CO., Ltd., Hangzhou, China) following the manufacturer's protocol.

### 2.9. Sequence and primary analysis

Cutadapt software (https://cutadapt.readthedocs.io/en/stable/, version:cutadapt-1.9) was used to remove the reads that contained adaptor contamination (command line: ~cutadapt -a ADAPT1 -A ADAPT2 -o out1.fastq -p out2.fastq in1.fastq in2.fastq -O 5 -m 100). Subsequently, low-quality and undetermined bases were discarded, and we used HISAT2 software (https://daehwankimlab.github.io/hisat2/, version:hisat2-2.0.4) to map reads to the genome (for example: *Homo sapiens* Ensembl v96), (command line: ~hisat2 -1 R1.fastq.gz −2 R1. fastq.gz -S sample_mapped.sam). The mapped reads were assembled for each sample using StringTie (http://ccb.jhu.edu/software/stringtie/, version: stringtie-1.3.4d. Linux_x86_64) with default parameters (command line: ~ stringtie -p 4 -G genome.gtf -o output.gtf -l sample input. bam). A comprehensive transcriptome was then reconstructed by merging all sample transcriptomes using gffcompare software (http://ccb.jhu.edu/software/stringtie/gffcompare.shtml, version: gffcompare-0.9.8. Linux_ x86_64). After the final transcriptome was generated, StringTie and ballgown (http://www.bioconductor.org/packages/release/bioc/html/ballgown.html) were used to estimate the expression levels of all transcripts and perform expression level for mRNAs by calculating FPKM (FPKM = [total_exon_fragments/mapped_reads(millions) × exon _length (kB)]), (command line: ~stringtie -e -B -p 4 -G merged.gtf -o samples.gtf samples. bam). Differentially expressed mRNAs, defined by a fold change >2 or <0.5 and a p-value <0.05, were identified using the R package edgeR (https://bioconductor.org/packages/release/bioc/html/edgeR.html) and DESeq2 (http://www. bioconductor. org/packages/release/bioc/html/DESeq2. html). Enrichment analyses for Gene Ontology (GO) and Kyoto Encyclopedia of Genes and Genomes (KEGG) pathways were subsequently performed on these mRNAs.

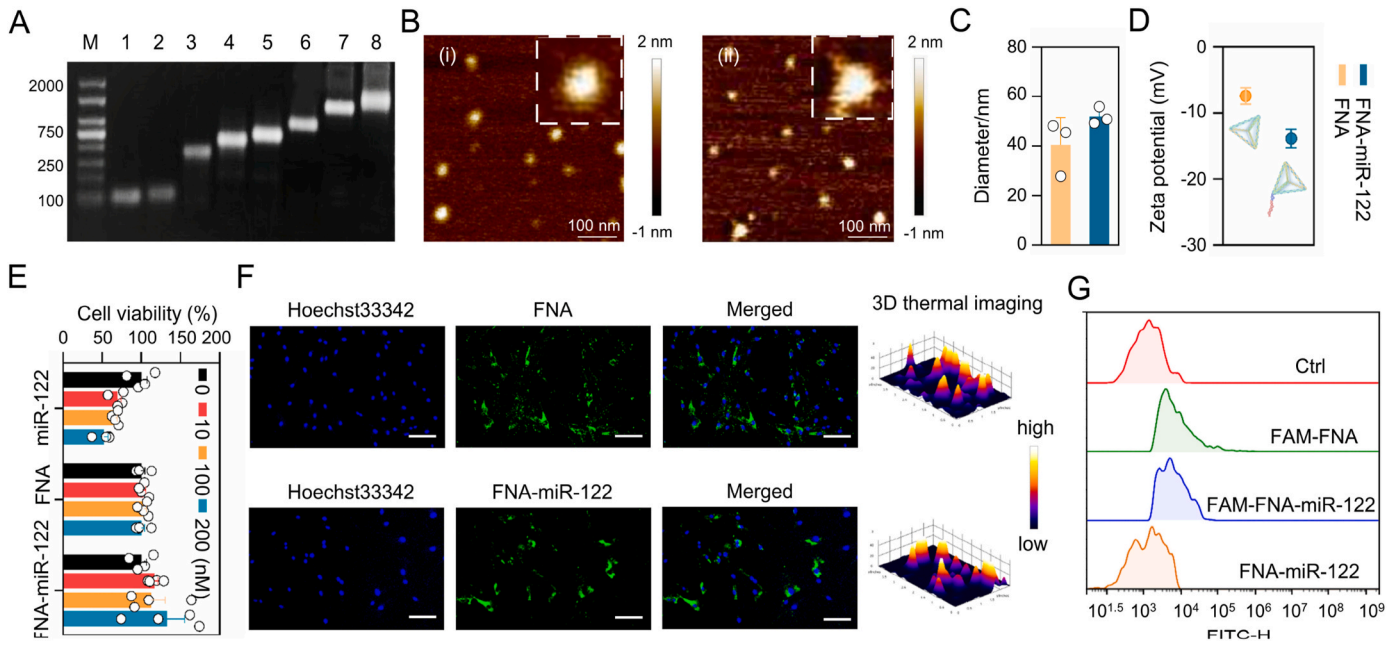


**Fig. 1.** Characterization and cellular uptake of FNA and FNA-miR-122. (A) Agarose gel electrophoresis (2%) illustrating the precise self-assembly process of FNA-miR-122 (M: Marker, Line 1: miR-122, Lines 2–7: $T_1$, $T_1$+$T_2$, $T_1$+$T_2$+$T_3$, $T_2$+$T_3$+$T_4$, $T_1$+$T_3$+$T_4$, and $T_1$+$T_2$+$T_3$+$T_4$ representing FNA, Line 8: FNA-miR-122). (B) AFM morphological characterizations of FNA (i) and FNA-miR-122 (ii). (C) Hydrodynamic diameters of FNA and FNA-miR-122. Data are represented as mean ± standard deviation (SD) (n = 3). (D) Zeta potential distributions of FNA and FNA-miR-122 (n = 3). (E) Cellular viability of ADMSCs treated with miR-122, FNA, and FNA-miR-122 at various concentrations (n = 4). (F) Confocal laser scanning microscopy (CLSM) images showing uptake of FNA and FNA-miR-122 in ADMSCs after 6 h of incubation with FAM as a fluorescence probe (scale bars: 50 μm). Green: FAM-labeled FNA and FNA-miR-122; blue: Hoechst 33342-stained nuclei. (G) Flow cytometry analysis estimating the cellular uptake efficiency of FNA and FNA-miR-122 in ADMSCs after 2 h.

### 2.10. Endothelial cell culture

Human umbilical vein endothelial cells (HUVECs) were obtained commercially and cultured under conditions of 37 °C, 5 % $CO_2$ in an endothelial cell growth medium (Saliai Stem cell Science and Technology Co., LTD, Guangzhou, China). The maintenance involved passaging HUVECs at 80% confluency and restricting use to within five passages for all experimental protocols.

### 2.11. Generation of cell spheroids

FNA-miR-122-iHeps (Heps) were mixed with HUVECs (HUEs) in various ratios (1:0, 1:1, 4:1, 9:1) and cultured in 96-well U-bottom plates to generate co-culture cell spheroids. These liver spheroids were cultured in the U-bottom plates for 3 days. After that, the biofunctions of the cell spheroids were investigated.

### 2.12. Calcein-AM/PI double staining assay

A stock solution of Calcein-AM (Aladdin) was prepared by dissolving the dye in dimethyl sulfoxide (DMSO) to achieve a concentration of 1 mM. This solution was subsequently diluted to 1–50 μM with PBS. Similarly, the propidium iodide (PI) stock solution (Solarbio) was diluted with PBS to concentrations ranging from 10 to 50 μM. The cell spheroids were treated with the working solutions of calcein-AM and PI for 10–15 min. The images were captured using an inverted fluorescence microscope (Axio Observer 3, Zeiss), with excitation wavelengths at 488 nm and 561 nm.

### 2.13. Transplantation of FNA-miR-122-iHep into mice with ALF

All animal experiments were conducted following the protocol approved by the Institutional Animal Care and Use Committee of Sun Yat-Sen University (SYSU-IACUC-2023-000523). The 5-week-old and 6-week-old male C57BL/6J mice were housed under sterile conditions in laminar flow cabinets with autoclaved food, water, bedding, and cages. ALF was induced by intraperitoneally injecting the mice with 4 μL/g (body weight) of $CCl_4$ dissolved in olive oil. The development of ALF was confirmed 24 h post-injection via histological and biochemical blood tests. Mice were then divided into six groups, with ten mice per group. The control group consisted of untreated male mice. 24 h after ALF induction, groups 2–6 were intravenously injected with 100 μL of 0.9 % saline as a negative control, hADMSCs ($5 \times 10^6$ cells/mice), FNA-ADMSCs ($5 \times 10^6$ cells/mice), miR-122-iHep ($5 \times 10^6$ cells/mice), FNA-miR-122-iHep ($5 \times 10^6$ cells/mice), respectively. The $CCl_4$-induced ALF mice with or without treatment were assessed on day 3 after cell transplantation. Subsequently, mice were euthanized, and major organs were harvested and fixed in 10 % neutral-buffered formalin for further analysis. Liver and kidney functions were compared to those of healthy control mice. To evaluate the therapeutic impact of FNA-miR-122-iHep on liver function in ALF mice, serum levels of alanine aminotransferase (ALT) and aspartate aminotransferase (AST) were measured. Additionally, liver samples were processed for hematoxylin and eosin (H&E) staining, and immunohistochemical analysis of nuclear protein Ki67, terminal deoxynucleotidyl transferase dUTP nick end labeling (TUNEL), reactive oxygen species (ROS), and tumor necrosis factor-α (TNF-α).

### 2.14. In vivo fluorescence imaging

Briefly, the DiD-labeled FNA-miR-122-iHep were administered into ALF mice via tail intravenously injection. Afterward, these mice were euthanized, and the major organs (heart, liver, spleen, lung, and kidney) were harvested for analysis. The noninvasive NIR fluorescence imaging system (IVIS Lumina LT Series III, PerkinElmer, USA) that consists of an excitation light source and a cold charge-coupled device (CCD) was used for tissue fluorescence imaging. The system featured a characteristic fluorescence with an excitation and emission wavelength at 640 nm and 700 nm, respectively.

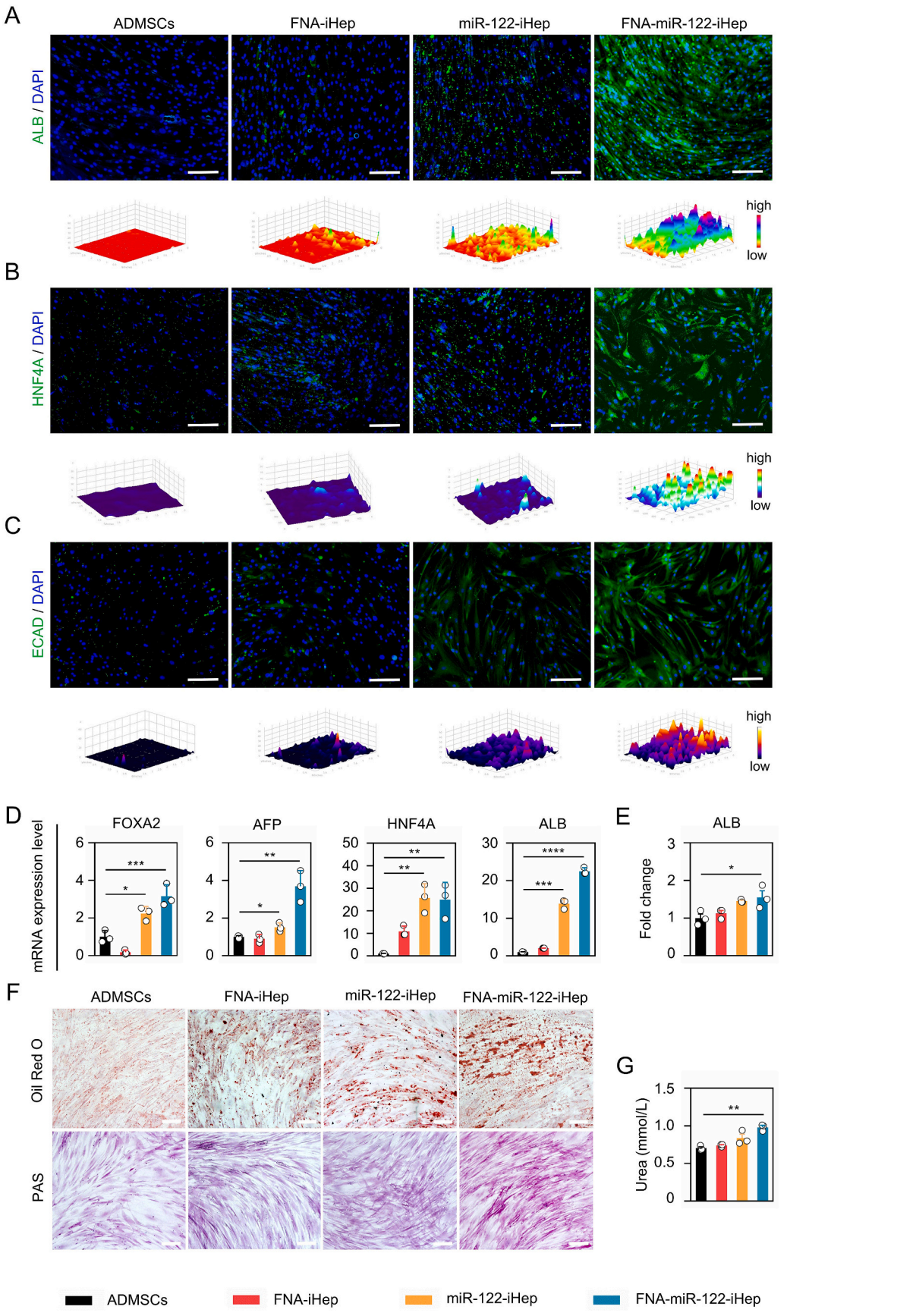


*(caption on next page)*

**Fig. 2.** FNA-miR-122 stimulates hepatic differentiation of ADMSCs. (A) Immunofluorescent staining and 3D spectrum plot showing ALB expression in FNA-miR-122-iHeps at day 21. Nuclei were stained with DAPI (scale bar: 100 μm). (B) Immunofluorescent staining and 3D spectrum plot of HNF4A expression in FNA-miR-122-iHeps at day 21. Nuclei were stained with DAPI (scale bar: 100 μm). (C) Immunofluorescent staining and 3D spectrum plot depicting ECAD expression in FNA-miR-122-iHeps at day 21. Nuclei were stained with DAPI (scale bar: 100 μm). (D) The mRNA expression levels of hepatocyte-specific marker genes (FOXA2, AFP, HNF4A, ALB) in differentiated cells at 21 days. (E) Measurement of albumin secretion after 21 days in differentiation medium, with statistical significance indicated by asterisks (n = 3). (F) Oil Red O and periodic acid-Schiff (PAS) staining highlighting lipid production and glycogen storage, respectively, in the FNA-miR-122-iHeps (scale bar: 100 μm). (G) Urea detection in the cell culture medium of FNA-miR-122-iHep after 21 days, with statistical significance indicated by asterisks ( n = 3).

### 2.15. In vivo implantation of hepatic spheroids

The ALF animal model was established as previously described. Hepatic spheroids, comprising approximately 160–180 units ($8 \times 10^5$ - $9 \times 10^5$ cells), were implanted into the mesentery of male C57BL/6J mice aged 5–6 weeks and secured with fibrin gel. The mice were randomly assigned to five groups: a healthy control group (Health), an ALF model group (ALF), and three treatment groups: ALF treated with hepatocytes (Hep), ALF treated with hepatic-liver spheroids (Hep-Liver spheroids), and ALF treated with Hep:HUE-liver spheroids (Hep:HUE-Liver spheroids). Therapeutic outcomes were evaluated 2 days post-implantation. Upon completion of the assessment, the mice were euthanized, and organ sections were fixed in 10 % neutral-buffered formalin for further functional analyses. Additionally, in vivo transplantation of hepatic spheroids was also performed on male BALB/c nude mice aged 5–6 weeks for further therapeutic effect studies.

To evaluate the therapeutic effect and biosafety, histological and histopathological analyses were performed using a histology microscope (Olympus DX45, Japan). For frozen tissue staining, 10 μm thick liver cryosections were fixed in 4 % paraformaldehyde and permeabilized/blocked. To identify proliferating cells in liver tissue, the slides were incubated with the anti-Ki-67 (1:100) antibody, followed by counterstaining with DAPI for nuclear visualization. Apoptosis was assessed using TUNEL staining alongside DAPI counterstaining. In addition, liver samples were processed for immunohistochemical analysis of ALB, VEGF, LY6G, and other markers. To evaluate the therapeutic efficacy, ALT, AST, albumin (Alb), as well as kidney-associated serum urea nitrogen (Urea), and serum creatinine (Cre) toxicity were measured. Moreover, the main cytokines (IL-6, TNF-α, iNOS, IL-1β, and IL-10) as the systemic inflammation markers were analyzed.

### 2.16. Statistical analyses

All statistical data were analyzed using GraphPad Prism 6.0 (GraphPad Software, La Jolla, CA). Results were represented as mean ± standard deviation (SD) from at least three separate experiments to ensure statistical validity. A one-way analysis of variance (ANOVA) test and Two-tailed Student's t-test were used as appropriate. The statistical significance was indicated using bars and asterisks, with $^{*}P < 0.05$, $^{**}P < 0.01$, $^{***}P < 0.001$, $^{****}P < 0.0001$, and ns denoting no significant difference.

## 3. Results and discussion

### 3.1. Characterization of the FNA-miR-122 nanoassembly

The functional FNA nanorobotic assembly was synthesized using four specifically designed ssDNAs ($T_1$, $T_2$, $T_3$, and $T_4$) by highly specific base complementary sequence pairing (Table S1). To load the miR-122 onto the FNA, the 3' sticky ends of ssDNAs endowed the FNA with one sticky-end apex. The miR-122 duplex bearing the sticky-end bearing passenger strand was incubated with FNA in a 1:1 ratio to create a stable FNA-miR-122 structure. The successful synthesis of FNA and FNA-miR-122 was verified by native polyacrylamide gel electrophoresis, which displayed distinct DNA assembly bands under ultraviolet (UV) illumination (Fig. 1A). The morphological characteristics of FNA nanoparticles and FNA-miR-122 were similar by atomic force microscopy (AFM) (Fig. 1B). Additionally, dynamic light scattering (DLS) analysis suggested that miR-122 loading increased the particle size of FNA, with average hydrodynamic diameters measured at 40.48 ± 11.06 nm for FNA and 52.00 ± 3.43 nm for FNA-miR-122, respectively (Fig. 1C). The zeta potential of FNA-miR-122 (−13.87 ± 1.40 mV) was lower compared to FNA alone (−7.45 ± 1.22 mV), likely due to the negative charge of the nucleic acid molecules (Fig. 1D). After being loaded on FNA, an obvious band representing intact miR122 in the FNA-miR-122 was apparent after incubation with 10 % FBS for 2 h, whereas the free miR-122 was almost completely degraded, indicating enhanced stability of the miR-122 when loaded onto FNA (Fig. S1).

To determine the suitability of FNA for miR-122 transport in living organisms, we then evaluated the biocompatibility of FNA-miR-122 when co-cultured with ADMSCs. CCK-8 assay results indicated that cells treated with miR-122 alone showed reduced viability, whereas cells exposed to three different concentrations of FNA and FNA-miR-122 displayed no toxicity, suggesting that FNA could mitigate the toxic effects of miR-122 (Fig. 1E). Confocal laser scanning microscopy (CLSM) confirmed that both FAM-labeled FNA and FNA-miR-122 were effectively internalized by ADMSCs, evidenced by strong fluorescence signals after 6 h of incubation (Fig. 1F). Notably, FAM-FNA-miR-122 was able to escape from lysosomes, preventing endo-/lysosomal degradation, as demonstrated by the separation of green and red fluorescence after 12 h (Fig. S2). Furthermore, flow cytometry (FACS) analysis revealed substantial shifts in fluorescence signals within ADMSCs, indicating effective cellular uptake of FNA-miR-122 (Fig. 1G). The internalization dynamics were further explored using endocytosis inhibitors, with FNA-miR-122 fluorescence reduced to 56.8 % ± 13.0 % in the presence of CPZ (a clathrin-mediated endocytosis inhibitor) and to 24.6 % ± 1.1 % with EIPA (an inhibitor of macropinocytosis), suggesting predominant internalization through micropinocytosis and clathrin-mediated pathways (Figs. S3A and S3B). This pattern aligns with prior findings on the critical roles of these pathways in the endocytosis of DNA nanomaterials (Fig. S3C) [41]. Collectively, FNA-miR-122 with excellent biocompatibility showed efficient cellular uptake, which was critically important for downstream hepatic differentiation.

### 3.2. FNA-miR-122-induced differentiation of ADMSCs to hepatocyte-like cells

As depicted in Scheme 1, the FNA-miR-122, serving as an unprecedented and potential platform, is expected to promote the ADMSCs hepatic differentiation process. Evaluations conducted revealed that, compared to untreated ADMSCs, those treated with FNA-miR-122 (FNA-miR-122-iHep) exhibited the transformation from spindle-like cells to polygonal and circular morphology at day 21 (Fig. S4). With regard to hepatocyte marker proteins, albumin (ALB) was specific for mature hepatocytes [42] and hepatocyte nuclear factor 4 alpha (HNF4A) was the most critical fate hepatic transcription factor [43]. As expected, ALB and HNF4A showed significantly enhanced expression in protein levels after 21 days of differentiation induced by FNA-miR-122 (Fig. 2A and B), which confirmed typical hepatic functional features of FNA-miR-122-iHep. Additionally, there was a marked increase in the expression of epithelial membrane protein marker E-cadherin (ECAD) in FNA-miR-122-iHep (Fig. 2C), which is known to respond to mechanical strain deformations in cell aggregates [44]. Quantitative real-time polymerase chain reaction (qRT-PCR) analysis further confirmed significant upregulation of hepatic marker-related genes in the FNA-miR-122-iHep group compared to the ADMSCs group (Fig. 2D).

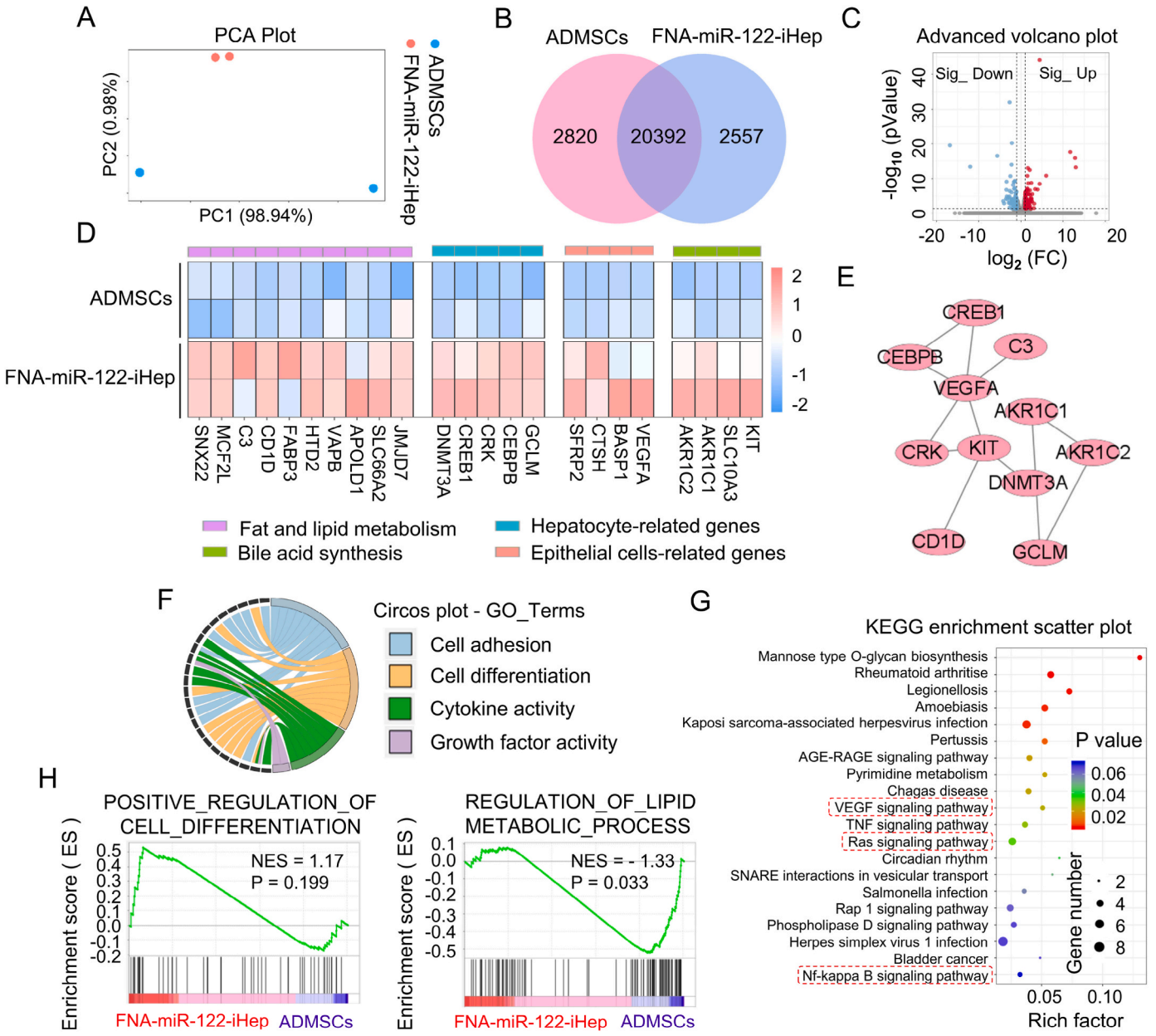


**Fig. 3.** Transcriptome analysis demonstrating FNA-miR-122-induced hepatic differentiation. (A) Principal component analysis (PCA) based on transcriptomic datasets from ADMSCs and FNA-miR-122-iHep groups. (B) Venn diagram of mRNAs differentially expressed in ADMSCs groups and FNA-miR-122-iHep groups. (C) Volcano plot illustrating gene expression differences between ADMSCs and FNA-miR-122-iHep groups. Blue points indicate significantly downregulated genes with a fold change >2, red points indicate upregulated genes with a fold change >2, and gray points show no significant difference. (D) Heatmap of gene expression related to specific liver functions such as hepatocyte-related genes, bile acid synthesis, epithelial cell-related genes, and fat and lipid metabolism in FNA-miR-122-iHep groups. (E) Protein-protein interaction (PPI) network of genes related to hepatic function and metabolism. (F) Gene ontology (GO) enrichment analysis of the subordination between the representative DEGs and their enriched pathways. (G) Bubble charts showing the KEGG pathway analysis results of differentially expressed genes (Top 20 KEGG pathways of DEGs). (H) Enrichment plots from GSEA analyses for gene sets associated with "POSITIVE_REGULATION_OF_CELL_DIFFERENTIATION" and "REGULATION_OF_LIPIDMETABOLIC_PROCESS". NES, normalized enrichment score. FDR, false discovery rate. Significant differences are indicated by |NES| (normalized enrichment score) > 1 and FDR (false discovery rate) q-value <0.25.

Especially, the expression of FOXA2, a marker for hepatic endoderm [45], was efficiently activated in FNA-miR-122-iHep cells, whereas the FNA-iHep was hardly affected. Similarly, the gene expression of ALB was greatly upregulated to 22.5-fold in the FNA-miR-122-iHep group as compared with the ADMSCs group. Meanwhile, the expression of alpha fetoprotein (AFP) [46] showed a progressive change in gene expression from ADMSCs to hepatocyte-like cells. Furthermore, functional analysis revealed substantial accumulations of fatty droplets and glycogen synthesis in the differentiated FNA-miR-122-iHep group, significantly surpassing those in the FNA-iHep and miR-122-iHep groups (Fig. 2F). Staining with periodic acid-Schiff (PAS) and oil red O showed strong positivity in the FNA-miR-122-iHep group, unlike the weaker staining observed in other groups. Notably, FNA-miR-122-iHep also confirmed the competency for the albumin (Fig. 2E) and urea secretion (Fig. 2G) by ELISA analysis. Collectively, these results demonstrated that FNA-miR-122 could directionally induce and activate the hepatic differentiation of ADMSCs, suggesting that FNA-miR-122-iHep can reliably produce hepatocyte-like cells with characteristic hepatic functions.

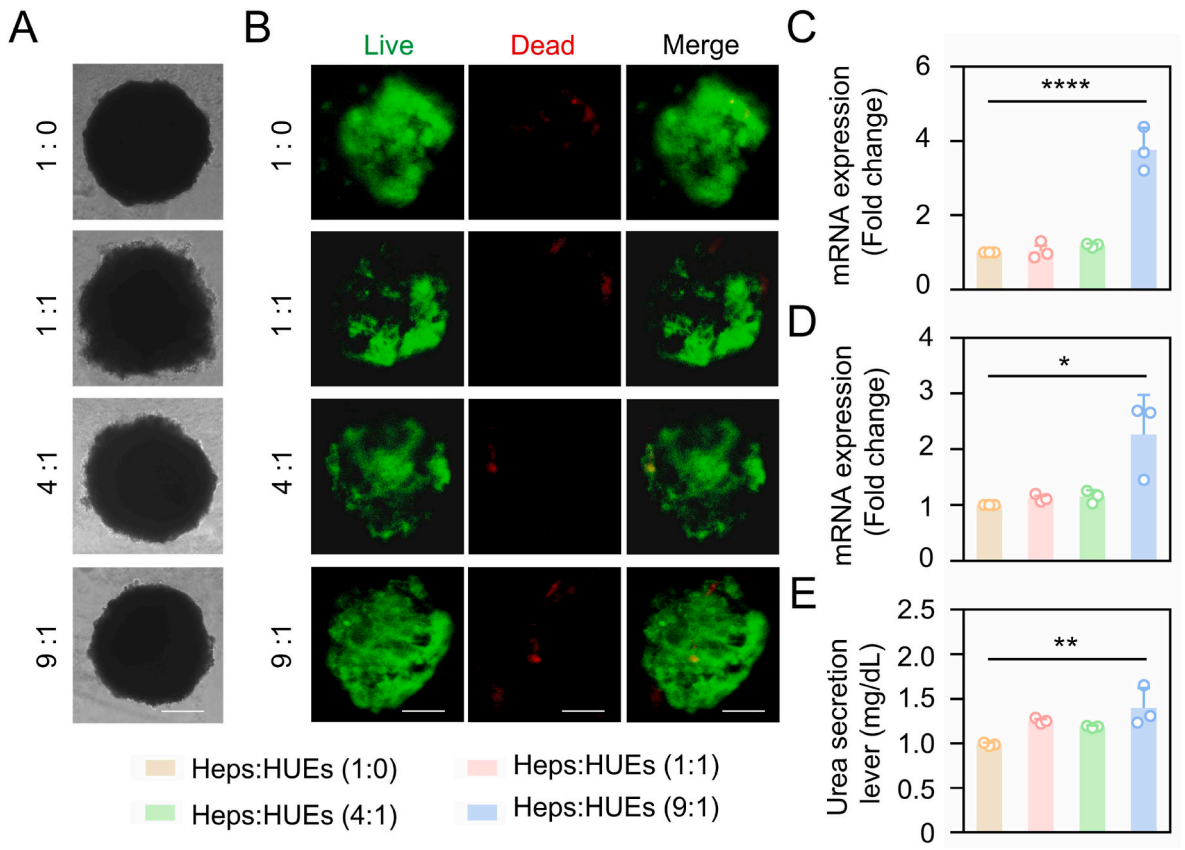


**Fig. 4.** Selection and characterization of functional liver spheroids from FNA-miR-122-iHep (Heps) and endothelial cells (HUEs). (A) Representative bright-field images of a single liver spheroid at day 3. The cell ratios of Heps to HUEs were 1:0, 1:1, 4:1, and 9:1 (Scale bar: 100 μm). (B) Cell viability assessed by live/dead staining after 3 days in culture, with green and red fluorescence indicating live and dead cells, respectively (scale bar: 100 μm). (C–D) mRNA expression levels of hepatocyte-specific markers (ALB and HNF4A) in liver spheroids, determined by qRT-PCR analysis (n = 3). (E) Detection of Urea in the cell culture medium of liver spheroids at different cell ratios of Heps to HUEs (1:0, 1:1, 4:1, 9:1).

### *3.3. Molecular mechanisms of hepatic differentiation induced by FNA-miR-122*

Ribonucleic acid sequencing (RNA-Seq) plays a pivotal role in unraveling the function and structure of genomes, elucidating genetic networks within cellular and physiological systems, and identifying novel molecular targets and biomarkers for medical and biopharmaceutical applications [47]. To further investigate molecular biological mechanisms by which FNA-miR-122 regulates hepatic differentiation in ADMSCs, RNA-Seq and transcriptome analysis were performed. Principal component analysis (PCA) analysis was utilized to differentiate the transcriptomic profiles of ADMSCs and FNA-miR-122-iHep (Fig. 3A). Analysis of the transcriptome data revealed that 20392 genes were co-expressed in both groups, while 2557 genes were exclusively expressed in the FNA-miR-122-iHep groups (Fig. 3B). Furthermore, a heatmap was plotted to illustrate the distinct expression patterns of the representative differentially expressed genes (DEGs) (Fig. S5). As shown in Fig. 3C, compared to the hADMCs group, the FNA-miR-122-iHep group had 124 upregulated genes and 137 downregulated genes. Gene Ontology (GO) enrichment analysis found that the DEGs caused by FNA-miR-122-iHep were mainly enriched in 25 biological processes (Fig. S6), which were crucial for FNA-miR-122-mediated hepatic differentiation.

Moreover, the gene expression of representative proteins and enzymes related to liver function and metabolism, including those involved in bile acid synthesis and secretion, hepatic-specific transcription factors, epithelial cell markers, and fat and lipid metabolism, were validated and confirmed to be significantly upregulated in FNA-miR-122-iHep group (Fig. 3D). These changes contributed to hepatic maturation during ADMSCs' differentiation. Meanwhile, according to Gene Set Enrichment Analysis (GSEA), FNA-miR-122 positively contributed to regulating the differentiation of ADMSCs (Fig. 3H). In addition, FNA-miR-122-iHeps also influenced the lipid metabolic processes (Fig. 3H). In contrast, the stem/progenitor cell-related genes were downregulated significantly (Fig. S7), further indicating a shift towards hepatic differentiation of ADMSCs after the FNA-miR-122 treatment. Concurrently, protein-protein interaction (PPI) network analysis of DEGs associated with bile acid synthesis, hepatic-specific transcription factors, and lipid metabolism, conducted using the STRING database, revealed functional interconnections among these proteins (Fig. 3E), further substantiating the role of FNA-miR-122 in promoting hepatic differentiation.

Afterward, the circos plot focused on the subordination of 124 upregulated representative DEGs and their enriched molecular functions, including "cell adhesion", "cell differentiation", "cytokine activity" and "growth factor activity", accounting for over 50 % of all the DEGs (Fig. 3F). As depicted in Fig. S8, the expression levels of the miR-122 target genes, including insulin-like growth factor receptor 1 (IGF1R), cyclin G1 (CCNG1), and prolyl-4-hydroxylase a1 (P4HA1), were elevated. Additionally, GO enrichment and Kyoto Encyclopedia of Genes and Genomes (KEGG) enrichment analyses were used to identify the key potential biological processes and pathways involved. GO analysis highlighted that the FNA-miR-122 could induce positive regulation of cell differentiation (Fig. S9). Particularly, "positive regulation of angiogenesis", "positive regulation of endothelial cell chemotaxis by VEGF (vascular endothelial growth factor)" and "vascular endothelial growth factor receptor-2 signaling pathways" might be involved in hepatic differentiation of ADMSCs into iHeps and hepatic regeneration. In

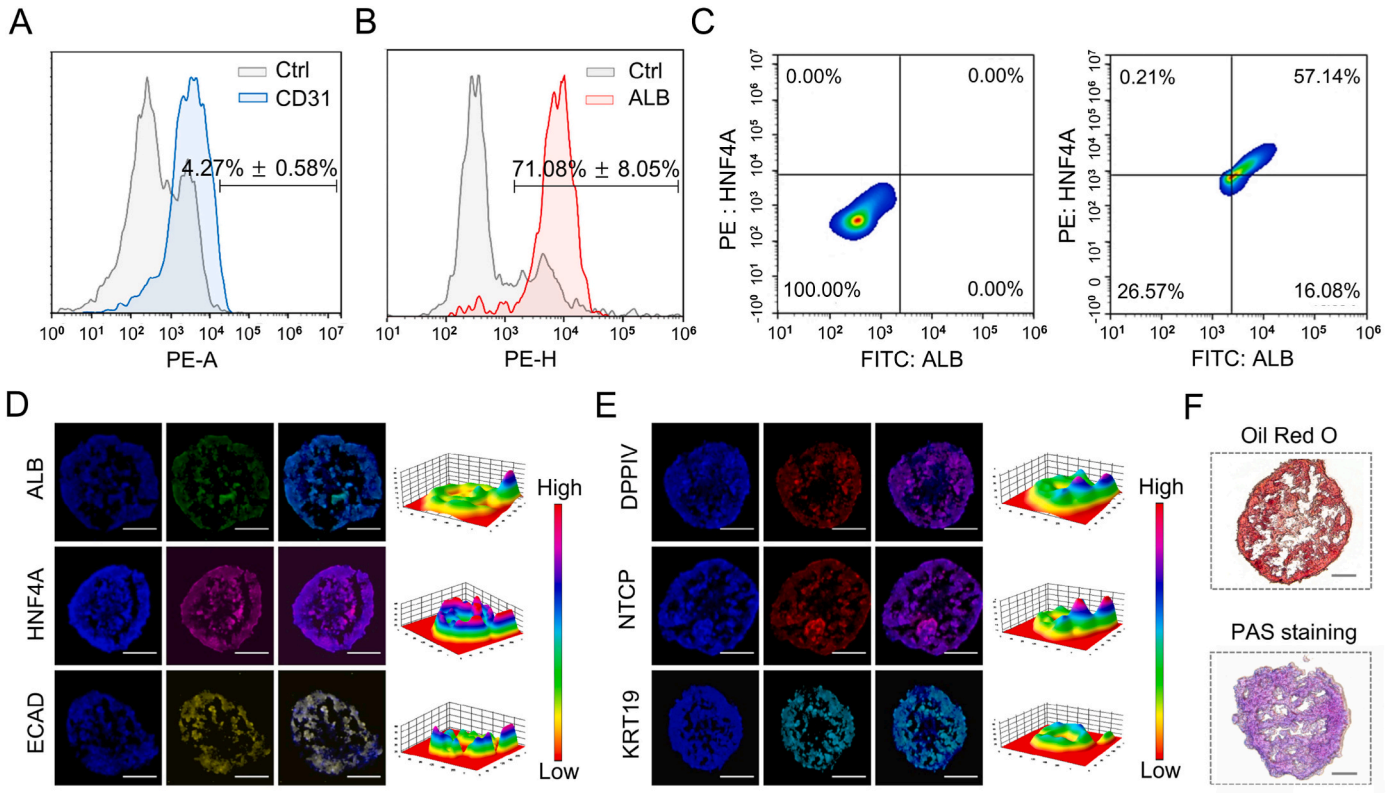


**Fig. 5.** Molecular characterization of cell spheroids. (A–B) Flow cytometry analysis confirming the proportion of endothelial cells (CD31) and iHeps (ALB) in liver spheroids. (C) Flow cytometry analysis of hepatocyte-specific markers (ALB and HNF4A) in liver spheroids. (D) Immunostaining for hepatocyte-specific markers (ALB, HNF4A, and ECAD) in liver spheroids (scale bars: 100 μm). (E) Immunostaining of apical (DPPIV), basolateral (NTCP) markers, along with the mature hepatocyte marker (KPT19) in liver spheroids. (F) Visualization of lipid droplets stained red with Oil Red O and glycogen synthesis indicated by periodic acid-Schiff (PAS) staining in liver spheroids (scale bar: 100 μm).

addition, KEGG pathway enrichment analysis further indicated that multiple pathways were associated with FNA-miR-122-induced hepatic differentiation, including the VEGF signaling pathway [48], MAPK signaling pathway [49], and TGF-β (transforming growth factor beta) signaling pathway [50] and so on (Fig. 3G). These findings align with previous research [51], suggesting that the interaction of these multi-level signaling pathways could underpin the molecular mechanisms driving hepatic differentiation induced by FNA-miR-122. Collectively, transcriptome analysis supported the potential of the FNA-miR-122-iHeps as the viable source of functional hepatocytes for cell therapy in liver diseases.

### 3.4. Generation of hepatic spheroids from FNA-miR-122-iHeps

Prior to the co-culture experiments, FNA-miR-122-iHeps (Heps) were mixed with HUVECs (HUEs) in various ratios (1:0, 1:1, 4:1, 9:1) and cultured in 96-well U-bottom plates to generate co-culture cell spheroids. The impacts of these ratios on hepatic biofunctions of cell spheroids were then assessed. As presented in Fig. 4A, the average size of the liver spheroids was determined to be approximately 200 μm by phase contrast microscopy. These liver spheroids represented excellent cell viability after culture for 3 days (Fig. 4B). Afterward, relative mRNA expression levels of mature hepatocyte-specific markers in the co-culture liver spheroids were examined, including ALB (Fig. 4C) and HNF4A (Fig. 4D). In addition, the Urea secretions in different groups were also measured (Fig. 4E). Results indicated that the liver spheroids significantly improved liver functions and exhibited optimal hepatocyte performance when the ratio of Heps and HUEs was 9:1, which was selected for further co-culture spheroid studies. Furthermore, we also tracked the expression of miR-122 throughout the entire process of hepatic differentiation and hepatic spheroid formation. As depicted in Fig. S10, the miR-122 expression levels exhibited a gradual increase in the FNA-miR-122-iHeps group at 7, 14, and 21 days post-transduction, as compared to the undifferentiated ADMSCs (day 0). Additionally, following the formation of the Hep:HUE-Liver spheroids, there was a further enhancement in miR-122 expression.

### 3.5. Evaluation of the hepatic function in the hepatic spheroids in vitro

The composition and functional status of cells within liver spheroids were analyzed using fluorescence-activated cell sorting. The results showed that approximately 4.27 % ± 0.58 % of the cells expressed the mature vascular endothelial marker CD31 [53] (Fig. 5A), and 71.08 % ± 8.05 % cells positively expressed the mature hepatic markers ALB (Fig. 5B) in hepatic spheroids after 3 days of 3D culture. Moreover, flow cytometry and immunofluorescence assays confirmed the co-expression of ALB and HNF4A, indicating the maturation of Heps into functional hepatocytes in liver spheroids by day 3 (Fig. 5C). The improved hepatic biofunctions of liver spheroids might be attributed to the maintained hepatocyte polarity, as evidenced by high levels of ECAD proteins (Fig. 5D) [54]. In addition, the high expressions of basolateral membrane proteins NTCP and apical membrane proteins DPPIV [22] indicated the successful development of functional liver parenchyma within the spheroids (Fig. 5E). Immunofluorescence identified upregulation of early biliary specification markers KRT19 [43], demonstrating excellent hepatic function properties of liver spheroids during liver development (Fig. 5E). As illustrated in Fig. 5F, oil red O and PAS staining in liver spheroids further confirmed fatty droplet synthesis and glycogen accumulation, respectively. Overall, these findings suggested that differentiated Heps and HUEs within liver spheroids progressively matured, offering significant potential for liver disease therapy.

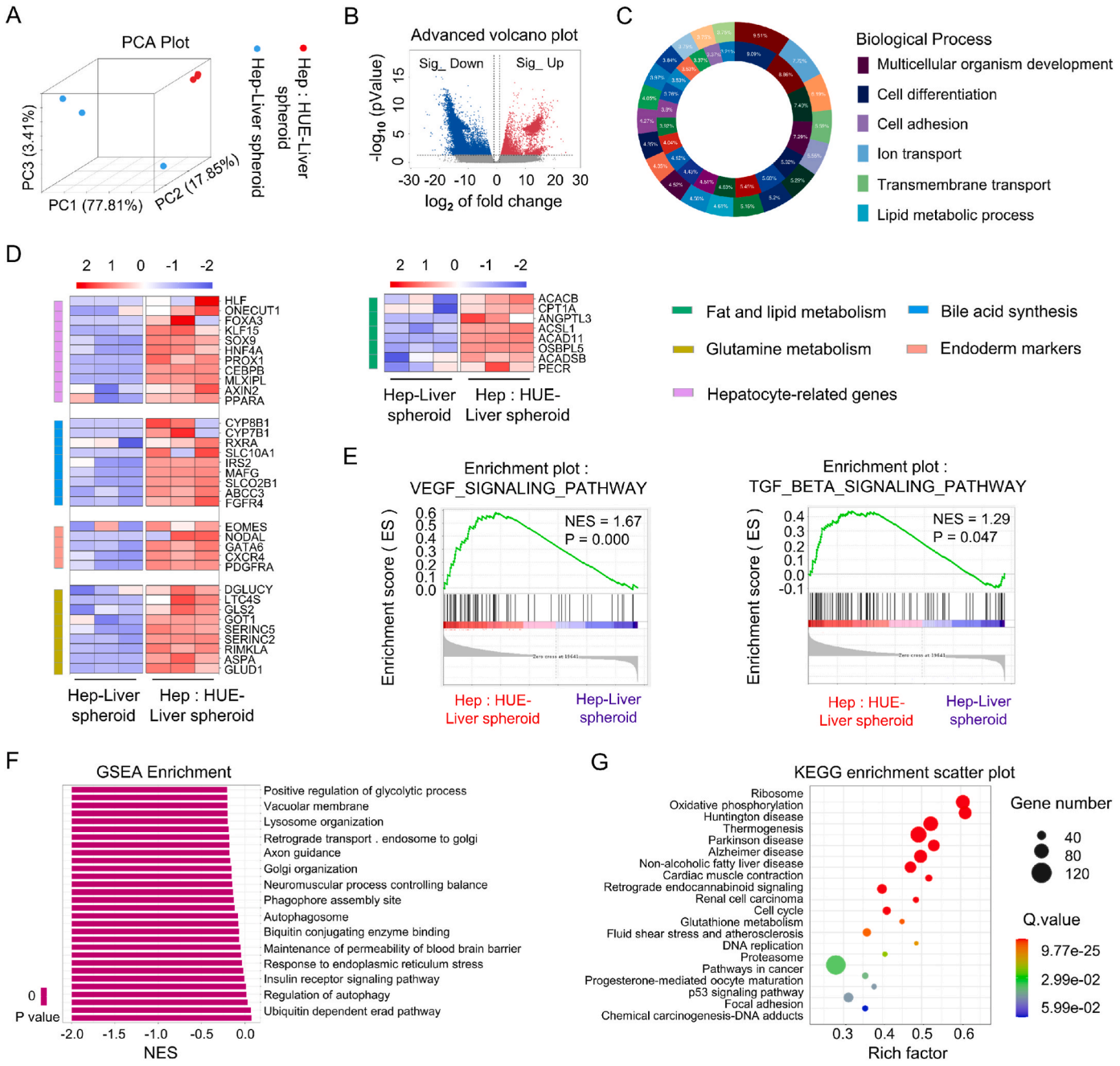


**Fig. 6.** Transcriptomic analysis of Hep:HUE-Liver spheroid at day 3. (A) PCA analysis based on transcriptomic datasets of Hep:HUE-Liver spheroid and Hep-Liver spheroid. (B) Volcano plots depicting gene expression differences between Hep:HUE-Liver spheroids in co-culture and Hep-Liver spheroids in mono-culture. Differentially expressed genes with a fold change >2.0 and $P < 0.05$ are highlighted: blue points indicate significantly downregulated genes, red points indicate significantly upregulated genes, and gray points indicate no significant difference. P values were calculated using a two-sided unpaired Student's t-test with equal variance assumed. (C) GO enrichment analysis of the subordination between the representative DEGs and their enriched biological process. (D) Heatmap displaying the expression of genes related to specific liver functions (fat and lipid metabolism, bile acid synthesis, hepatocyte-related genes, glutamine metabolism, endoderm markers) in Hep:HUE-Liver spheroid and Hep-Liver spheroid. (E) Enrichment plots from GSEA for "VEGF_SIGNALING_PATHWAY" and "TGF_BETA_SIGNALING_PATHWAY". (F) GSEA enrichment analysis comparing Hep:HUE-Liver spheroid to the Hep-Liver spheroid. |NES| > 1, FDR P value < 0.25 indicate significant differences between the groups. (G) KEGG Pathway enrichment analysis of the Hep:HU-Liver spheroid under mono- and co-culture conditions at day 3. Dot colors represent the rich factor, while sizes indicate the number of input genes for each KEGG term (Top 20 KEGG pathways of DEGs).

### *3.6. Transcriptional analysis of Hep:HUE-Liver spheroids*

To elucidate the diverse physiological responses of Hep:HUE-Liver spheroids within the co-culture system, RNA-Seq analysis was conducted on the third day of culture under both mono- and co-culture conditions. PCA highlighted significant transcriptomic differences between mono-cultured Hep-Liver spheroids and co-cultured Hep:HUE-Liver spheroids, suggesting a profound influence of the co-culture environment on liver spheroid development (Fig. 6A). A total of 7927 DEGs were identified in the co-cultured Hep:HUE-Liver spheroids, including 4445 upregulated and 3482 downregulated genes, which were earmarked for further analysis (Fig. 6B). Besides, hierarchical clustering demonstrated distinct gene expression profiles between the co-culture and mono-culture systems (Fig. S11), indicating that the co-culture

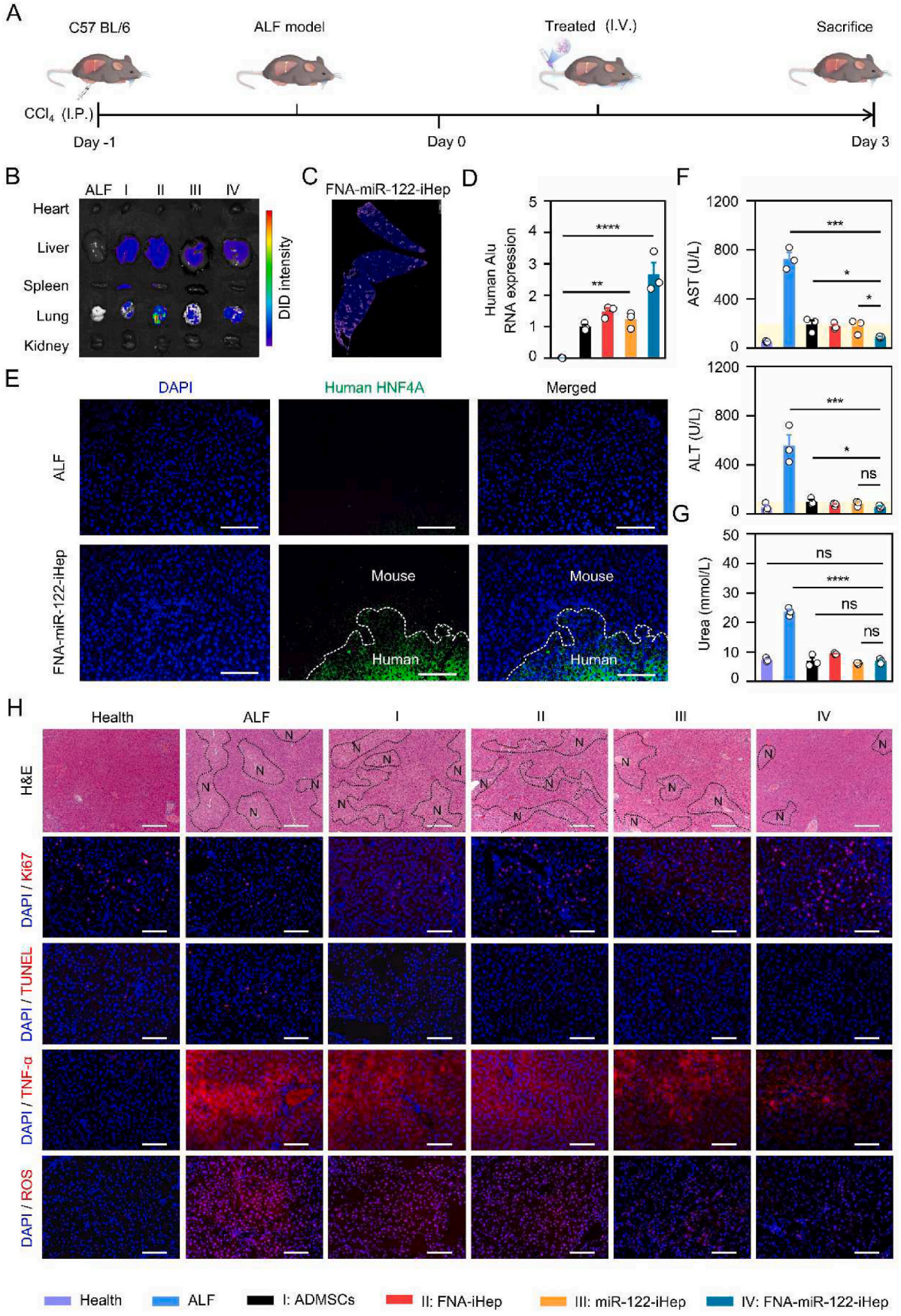


*(caption on next page)*

**Fig. 7.** In vivo therapeutic efficacy of FNA-miR-122-iHep in ALF mice. (A) Schematic of the administration treatment used in this study: intravenous injection (I.V.) and intraperitoneal injection (I.P.). (B) Fluorescence biodistribution images of various tissues (hearts, livers, spleens, lungs, and kidneys) 3 days post-intravenous injection of DiD-labeled ADMSCs, FNA-iHep, miR-122-iHep, and FNA-miR-122-iHep. (C) Distribution pattern of DiD-labeled FNA-miR-122-iHep within whole liver tissue. (D) The mRNA expression analysis of human Alu sequences for identification and quantification of human cells. (E) Immunofluorescent staining for hepatocyte marker human HNF-4α in liver tissue of the FNA-miR-122-iHep group (Scale bar: 100 μm). (F) Analysis of liver damage markers (alanine aminotransferase (ALT) and aspartate aminotransferase (AST)) in ALF mice post-treatment, displayed against a normal range (yellow background). (G) The detection of urea in the serum of mice after various treatments. (H) H&E staining (N, necrosis), Ki67-positive cells (red nuclei), TUNEL-positive cells (red nuclei), TNF-α and ROS levels in liver tissues from ALF mice treated with different groups at 3 days (Scale bar: 100 μm).

system showed significant impacts on liver function maturation of the resulting spheroids.

Subsequent DEG analysis revealed that the DEGs caused by Hep:HUE-Liver spheroids were enriched in six biological processes, including "multicellular organism development", "cell differentiation", "cell adhesion", "ion transport", "transmembrane transport" and "lipid metabolic process" (Fig. 6C). These processes accounted for approximately 30 % of all DEGs and are thought to enhance hepatic differentiation and function in Hep:HUE-Liver spheroids relative to Hep-Liver spheroids. Further analyses of mature liver signature gene expression profiles showed higher expression levels in Hep:HUE-Liver spheroids compared to their mono-cultured counterparts (Fig. 6D). Notably, Hep:HUE-Liver spheroids displayed enhanced expression of genes involved in glutamine metabolism and endoderm development. The co-culture conditions evidently supported endodermal maturation, thereby augmenting liver function in the Hep:HUE-Liver spheroids compared to mono-cultured Hep-Liver spheroids.

Additionally, the GSEA analyses highlighted that Hep:HUE-Liver spheroids significantly participated in the fatty acid metabolism, positive regulation of the glycolytic process, sphingolipid metabolic process, blood vessel development and positive regulation of glycolytic process, and so on (Fig. 6F), indicating that Hep:HUE-Liver spheroids improved metabolic activities and viability of hepatocyte cells in Hep:HUE-Liver spheroids, which would be crucial for microliver formation and function [46]. Concurrently, GSEA identified upregulation in specific pathways in the Hep:HUE-Liver spheroid group, including the VEGF and TGF-β signaling pathways (Fig. 6E), which suggested that Hep:HUE-Liver spheroids could promote hepatic regeneration progression [22]. Notably, TGF-β is known to activate hepatic stellate cells and promote angiogenesis in vascular endothelial cells in vitro [20], which would support the development of vascularized and functional liver organoids from these co-cultured Hep:HUE-Liver spheroids.

Afterward, KEGG enrichment analysis was applied to determine the potential biological behaviors and pathways enriched among the significantly upregulated genes, revealing the activation of metabolically relevant signaling pathways in the co-cultured Hep:HUE-Liver spheroids (Fig. 6G and S12). Compared with Hep-Liver spheroids in mono-cultures, the co-culture system of the Hep:HUE-Liver spheroids enhanced several pathways such as drug metabolism cytochrome P450, amino sugar and nucleotide sugar metabolism, oxidative phosphorylation, glutathione metabolism, insulin signaling pathway, and sphingolipid signaling pathway, all of which were essential for regulating lipid metabolic activity, drug metabolism, liver homeostasis and insulin sensitivity [55]. Collectively, these data revealed the Hep:HUE-Liver spheroids in co-culture systems not only exhibited effective hepatic differentiation but also improved tissue-specific functions. Furthermore, the co-culture Hep:HUE-Liver spheroids in complicated surroundings would offer new mechanistic insights into the regulation of hepatic differentiation in terms of phenotypic adaptability and functional versatility.

### 3.7. Therapeutic efficacy of FNA-miR-122-iHep transplantation in an ALF mouse model

ALF, known for its rapid onset and high morbidity and mortality, presents significant therapeutic challenges. Motivated by the promising hepatic differentiation capabilities of FNA-miR-122-iHeps, we further investigated its therapeutic potential for ALF in vivo. The $CCl_4$-induced ALF mouse model was treated with FNA-miR-122-iHeps via tail vein injection, and the experimental procedures were outlined in Fig. 7A. In the model group treated solely with $CCl_4$, numerous white spots and extensive surface irregularities were observed in the liver (Fig. S13), along with elevated serum aspartate aminotransferase (AST) and alanine transaminase (ALT) levels (Fig. 7F), confirming successful model establishment. Following transplantation of FNA-miR-122-iHeps, notable improvements included smoother liver surfaces and tissue coloration resembling that of a normal liver. Additionally, DiD-stained cell tracking revealed that the labeled FNA-iHep, miR-122-iHep, and FNA-miR-122-iHep were predominantly presented in the lung and liver (Fig. 7B). Microscopic examination of the liver section from the treatment group showed widespread distribution of FNA-miR-122-iHeps across the liver (Fig. 7C), which further suggested that the FNA-miR-122-iHeps were able to successfully repopulate damaged livers. Simultaneously, qRT-PCR analysis indicated that the mRNA levels of human-specific Alu were markedly increased in the FNA-miR-122-iHep group, implying superior engraftment and proliferation of FNA-miR-122-iHeps compared to ADMSCs, FNA-iHeps, and miR-122-iHeps (Fig. 7D).

Subsequently, to assess the liver-specific functionality of the FNA-miR-122-iHeps, immunofluorescence analyses using anti-human-specific HNF4A antibodies were performed. The expression of human HNF4A protein (green) in mouse livers, as shown in Fig. 7E, confirmed the successful integration of FNA-miR-122-iHeps. Notably, ALT and AST levels in the FNA-miR-122-iHep group were more than twice as low as those in other treatment groups, underscoring its therapeutic superiority (Fig. 7F). Moreover, reductions in serum urea nitrogen (Fig. 7G) and creatinine levels (CREAT) (Fig. S14) indicated a protective effect of FNA-miR-122-iHeps on the liver, mitigating ALF-associated renal complications. Interestingly, the ADMSCs group also had a certain therapeutic effect compared with the model group [52].

Furthermore, hematoxylin and eosin (H&E) and immunofluorescence stainings were conducted to further confirm that the transplanted FNA-miR-122-iHeps could reduce liver injury in the ALF model. The TUNEL and Ki67 staining revealed that the FNA-miR-122-iHep group had the weakest apoptosis level and the highest proliferation ability among all groups (Fig. 7H). In addition, TNF-α was expressed at low levels in the FNA-miR-122-iHep groups compared to other treatment groups (Fig. 7H), implying that FNA-miR-122-iHeps exhibited excellent anti-inflammatory effects. What is more, ROS levels were reduced in the ADMSCs group compared to that in the ALF group, and further significantly decreased in the FNA-miR-122-iHep group (Fig. 7H), implying that the reduction in hepatocyte apoptosis and necrosis by FNA-miR-122-iHeps was partly due to its antioxidative action (Fig. S15). In addition, there were no signs of systemic toxicity in all the treatment groups (Fig. S16). Taken together, the transplantation of FNA-miR-122-iHep showed pronounced therapeutic benefits in treating ALF, primarily attributed to its anti-apoptotic, antioxidant, and anti-inflammatory effects, enhancing liver function recovery and reducing secondary organ damage.

### 3.8. Evaluation of therapeutic efficacy of hepatic spheroids in vivo

To assess the therapeutic benefits of liver spheroids in vivo, we implanted multiple spheroids over the mesenteric vascular beds in ALF-challenged mice (Fig. 8A). Compared to the ADMSCs and FNA-miR-122-

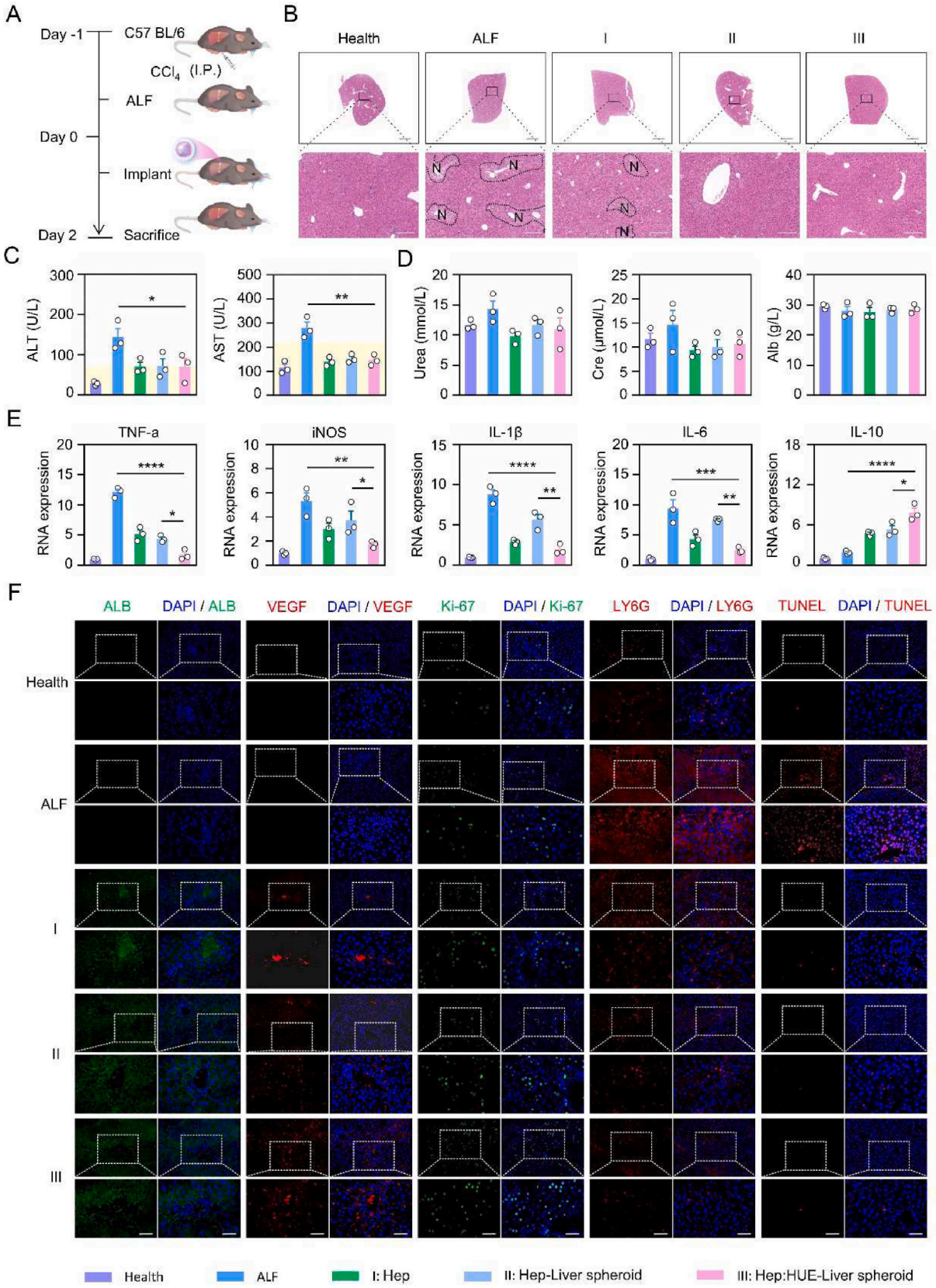


**Fig. 8.** Therapeutic potential of liver spheroids in C57BL/6 mice in vivo. (A) Schematic diagram of the experimental procedure. (B) H&E staining results 2 days post-transplantation of liver spheroids showing areas of necrosis (N). (C) Analysis of hematological markers of liver damage (ALT and AST) in ALF mice after different treatments, normal range (yellow background). (D) Detection of albumin and kidney damage markers (urea and creatinine) in serum from ALF mice post various treatments. (E) qRT-PCR measurement of mRNA expression of M1 (TNF-α, iNOS, IL-1β, IL-6) and M2 (IL-10) macrophage markers. (F) Immunofluorescent staining of liver tissue 2 days post-transplantation of liver spheroids. Markers stained include ALB, VEGF, Ki67, LY6G, and TUNEL in liver tissues from ALF mice treated with different groups (scale bar: 100 μm).

iHeps which were predominantly found in the lung and liver, the Hep:HUE-Liver spheroids were exclusively detected in the mesentery and exhibited no signal in other organs (Fig. S17). 2 days post-implantation, H&E staining of liver tissues showed that both the Hep-Liver and Hep:HUE-Liver spheroid-treated groups exhibited minimal necrosis and significant therapeutic effects, in stark contrast to the extensive necrotic damage observed in the ALF group (Fig. 8B). Additionally, AST and ALT levels were markedly reduced in the Hep:HUE-Liver spheroid-treated group compared to the ALF group on Day 2 (Fig. 8C). Notably, Hep:HUE-Liver spheroids reduced the expression of pro-inflammatory cytokines secreted by M1 macrophages (IL-6, TNF-α, iNOS, IL-1β, and COX-2) in liver tissue when compared to the Hep-Liver spheroids (Fig. 8E and S18). Conversely, these spheroids promoted significant secretion of the anti-inflammatory cytokine IL-10 by M2 macrophages, underscoring their superior hepatoprotective effects against ALF compared to Hep-Liver spheroid treatments. Analysis of urea nitrogen (Urea) and serum creatinine (Cre) levels showed no significant changes, indicating that renal function was unaffected by Hep:HUE-Liver spheroid treatment (Fig. 8D). Moreover, no significant morphological or histopathological abnormalities were observed in major organs (heart, spleen, lung, and kidney) in the Hep:HUE-Liver spheroids treatment group (Fig. S19), confirming that the treatment was free from serious side effects and systemic toxicity.

Immunofluorescence staining of liver tissue from the Hep:HUE-Liver spheroids treatment group demonstrated positive expression of ALB and VEGF (Fig. 8F), markers indicative of functional maturity and proangiogenic activity [27]. Further analysis using Ki67 immunofluorescence highlighted enhanced liver cell proliferation within the Hep:HUE-Liver spheroids treatment group. Additionally, evaluation of liver inflammation through Ly6G detection revealed a substantial reduction in immune cell infiltration in this group, suggesting a pronounced anti-inflammatory effect [56]. We also examined and compared the impact of FNA-miR-122-iHeps and Hep:HUE-Liver spheroids transplantation on the activation of tissue-resident macrophages (Figs. S20 and S21). Notably, the Hep:HUE-Liver spheroids group exhibited the most efficient macrophage polarization. Consistently, the TUNEL staining also showed markedly lower fluorescence signals in the Hep:HUE-Liver spheroids group compared to the ALF control, affirming the spheroids' capacity to protect hepatocytes from apoptosis. Furthermore, the extended treatment cycle of one week provided additional evidence of the efficacy of FNA-miR-122-iHeps and Hep:HUE-Liver spheroids in treating ALF (Fig. S22). Moreover, a separate model of ALF in nude mice further validated the robust therapeutic efficacy of Hep:HUE-Liver spheroids in vivo (Figs. S23–28). Collectively, these results indicate that Hep:HUE-Liver spheroids not only facilitate liver regeneration but also enhance liver function, highlighting their potential as a promising therapeutic tool for liver diseases.

## 4. Conclusion

In this study, we employed FNA-miR-122, noted for its biocompatibility and effective internalization, to induce hepatic differentiation of ADMSCs into FNA-miR-122-iHeps. This approach offers a straightforward and cost-effective method for generating functional hepatocytes in vitro. Transcriptome analysis provided insights into the potential molecular mechanisms of FNA-miR-122 in regulating the hepatic differentiation of ADMSCs. Further, we developed a co-culture system to construct Hep:HUE-Liver spheroids, enhancing the viability, liver function, and metabolic activities of the differentiated hepatocytes. Additional transcriptome analyses identified critical signaling pathways, such as VEGF and TGF-β, associated with the development of vascularized and functional hepatic organoids from Hep:HUE-Liver spheroids. In vivo studies demonstrated effective alleviation of ALF injuries through treatments with both FNA-miR-122-iHeps and Hep:HUE-Liver spheroid transplantation. These interventions could potentially offer an effective therapeutic strategy for liver transplantation and other liver diseases. Further exploration using large animal models and the development of treatment methods with more standardized production techniques are needed to confirm their potential for clinical translation.

## Ethics approval and consent to participate

All animal experiments were conducted following the protocol approved by the Institutional Animal Care and Use Committee of Sun Yat-Sen University (SYSU-IACUC-2023-000523).

## CRediT authorship contribution statement

**Hongyan Wei:** Writing – original draft, Methodology, Investigation, Formal analysis, Conceptualization. **Tiantian Xue:** Validation, Methodology. **Fenfang Li:** Methodology. **Enguo Ju:** Supervision, Software. **Haixia Wang:** Supervision, Software. **Mingqiang Li:** Supervision, Methodology, Conceptualization. **Yu Tao:** Writing – review & editing, Visualization, Validation, Supervision, Resources, Project administration, Methodology, Investigation, Conceptualization.

## Declaration of competing interest

The authors declare that they have no known competing financial interests or personal relationships that could have appeared to influence the work reported in this paper.

## Acknowledgements

This work is supported by the National Key Research and Development Program of China (2019YFA0111300), the Thousand Talents Plan, the Guangdong Provincial Pearl River Talents Program (2019QN01Y131), and the Medical Science and Technology Research Fund of Guangdong Province (A2022112).

## Appendix A. Supplementary data

Supplementary data to this article can be found online at https://doi.org/10.1016/j.bioactmat.2024.08.022.

## References

[1] X. Zhou, L. Cui, X. Zhou, Q. Yang, L. Wang, G. Guo, Y. Hou, W. Cai, Z. Han, Y. Shi, Y. Han, J. Cell Mol. Med. 21 (2017) 881–893.
[2] K. Takayama, M. Inamura, K. Kawabata, M. Sugawara, K. Kikuchi, M. Higuchi, Y. Nagamoto, H. Watanabe, K. Tashiro, F. Sakurai, T. Hayakawa, M.K. Furue, H. Mizuguchi, J. Hepatol. 57 (2012) 628–636.
[3] T. Yang, M. Poenisch, R. Khanal, Q. Hu, Z. Dai, R. Li, G. Song, Q. Yuan, Q. Yao, X. Shen, R. Taubert, B. Engel, E. Jaeckel, A. Vogel, C.S. Falk, A. Schambach, D. Gerovska, M.J. Araúzo-Bravo, F.W.R. Vondran, T. Cantz, N. Horscroft, A. Balakrishnan, F. Chevessier, M. Ott, A.D. Sharma, J. Hepatol. 75 (2021) 1420–1433.
[4] H. Jing, X. Zhang, K. Luo, Q. Luo, M. Yin, W. Wang, Z. Zhu, J. Zheng, X. He, Biomaterials 231 (2019) 119–131.
[5] X.-H. Xu, T.-J. Yuan, H.A. Dad, M.-Y. Shi, Y.-Y. Huang, Z.-H. Jiang, L.-H. Peng, Nano Lett. 21 (2021) 8151–8159.
[6] S. Li, Y. Liu, T. Tian, T. Zhang, S. Lin, M. Zhou, X. Zhang, Y. Lin, X. Cai, Small 17 (2021) 21–33.
[7] E. Huntzinger, E. Izaurralde, Nat. Rev. Genet. 12 (2011) 99–110.
[8] K.N. Ivey, D. Srivastava, Cell Stem Cell 7 (2010) 36–41.
[9] D. Bartel, Cell 136 (2009) 215–233.
[10] M. Ha, V.N. Kim, Nat. Rev. Mol. Cell Biol. 15 (2014) 509–524.
[11] D. Baek, J. Villén, C. Shin, F.D. Camargo, S.P. Gygi, D.P. Bartel, Nature 455 (2008) 64–71.
[12] Y. Chien, Y.-L. Chang, H.-Y. Li, M. Larsson, W.-W. Wu, C.-S. Chien, C.-Y. Wang, P.-Y. Chu, K.-H. Chen, W.-L. Lo, S.-H. Chiou, Y.-T. Lan, T.-I. Huo, S.-D. Lee, P.-I. Huang, Acta Biomater. 13 (2014) 228–244.
[13] J. Wu, J. Huang, S. Kuang, J. Chen, X. Li, B. Chen, J. Wang, D. Cheng, X. Shuai, Adv. Sci. 6 (2019) 1801809.
[14] S. Thakral, K. Ghoshal, Curr. Gene Ther. 15 (2014) 142–150.
[15] L. Zhang, X.-J.-N. Ma, Y.-Y. Fei, H.-T. Han, J. Xu, L. Cheng, X. Li, Pharmacol. Therapeut. 232 (2021) 108–114.
[16] Y. Min, S. Han, H. Ryu, S.-W. Kim, Cardiovasc. Res. 114 (2018) 1400–1409.
[17] I. Suhito, Y. Han, J. Min, H. Son, T.-H. Kim, Biomaterials 154 (2018) 223–233.

[18] A. MacDonald, R. Trotter, C. Griffin, A. Bow, S. Newby, W. King, L. Amelse, T. Masi, S. Bourdo, M. Dhar, J. Nanobiotechnol. 19 (2021) 285–303.
[19] J. Jang, H. Lee, Y.W. Eom, S. Kang, J. Park, J. Choi, H. Kim, Blood 108 (2006), 4251-4251.
[20] L. Li, J. Mu, Y. Zhang, C. Zhang, T. Ma, L. Chen, T. Huang, J. Wu, J. Cao, S. Feng, Y. Cai, M. Han, J. Gao, ACS Nano 16 (2022) 10811–10823.
[21] A. Chhabra, H.H.G. Song, K.A. Grzelak, W.J. Polacheck, H.E. Fleming, C.S. Chen, S. N. Bhatia, Proc. Natl. Acad. Sci. USA 119 (2022) e2115867119.
[22] D. Huang, S.B. Gibeley, C. Xu, Y. Xiao, O. Celik, H.N. Ginsberg, K.W. Leong, Adv. Funct. Mater. 30 (2020) 1909553.
[23] A. da Silva Morais, S. Vieira, X. Zhao, Z. Mao, C. Gao, J.M. Oliveira, R.L. Reis, Adv. Healthcare Mater. 9 (2020) 1901435.
[24] F. Rizvi, E. Everton, A.R. Smith, H. Liu, E. Osota, M. Beattie, Y. Tam, N. Pardi, D. Weissman, V. Gouon-Evans, Nat. Commun. 12 (2021) 613.
[25] E. Luce, A. Messina, J.C. Duclos-Vallee, A. Dubart-Kupperschmitt, Hepatology 74 (2021) 1101–1116.
[26] H. Koike, K. Iwasawa, R. Ouchi, M. Maezawa, K. Giesbrecht, N. Saiki, A. Ferguson, M. Kimura, W.L. Thompson, J.M. Wells, A.M. Zorn, T. Takebe, Nature 574 (2019) 112–116.
[27] H.C. Fiegel, P.M. Kaufmann, H. Bruns, D. Kluth, R.E. Horch, J.P. Vacanti, U. Kneser, J. Cell Mol. Med. 12 (2008) 56–66.
[28] J.J. Velazquez, R. LeGraw, F. Moghadam, Y. Tan, J. Kilbourne, J.C. Maggiore, J. Hislop, S. Liu, D. Cats, S.M. Chuva de Sousa Lopes, C. Plaisier, P. Cahan, S. Kiani, M.R. Ebrahimkhani, Cell Syst. 12 (2021) 41–55.e11.
[29] H.A. Reza, R. Okabe, T. Takebe, Transpl. Int. 34 (2021) 2031–2045.
[30] H.F. Chan, Y. Zhang, K.W. Leong, Small 12 (2016) 2720–2730.
[31] P. Kubinski, S. Ben-Shaul, S. Landau, A. Bajpai, B. Singh, J. Eager, A. Cohen, S. Levenberg, K. Spiller, Sci. Adv. 6 (2020) eaay6391.
[32] W. Fu, L. Ma, Y. Ju, J.G. Xu, H. Li, S.R. Shi, T. Zhang, R.H. Zhou, J.W. Zhu, R.X. Xu, C. You, Y.F. Lin, Adv. Funct. Mater. 31 (2021) 1–12.
[33] Y. Li, X. Zhang, X. Wan, X. Liu, W. Pan, N. Li, B. Tang, Adv. Funct. Mater. 30 (2020) 2000532.
[34] H. Thai, K.-R. Kim, K. Hong, T. Voitsitskyi, J.-S. Lee, C. Mao, D.-R. Ahn, ACS Cent. Sci. 6 (2020) 2250–2258.
[35] Y. Dong, C. Yao, Y. Zhu, L. Yang, D. Luo, D. Yang, Chem. Rev. 120 (2020) 9420–9481.
[36] S. Li, Y. Liu, T. Zhang, S. Lin, S. Shi, J. He, Y. Xie, X. Cai, T. Tian, Y. Lin, Adv. Mater. 34 (2022) e2204287.
[37] J. Zhu, Y. Yang, W. Ma, Y. Wang, L. Chen, H. Xiong, C. Yin, Z. He, W. Fu, R. Xu, Y. Lin, Nano Lett. 22 (2022) 2381–2390.
[38] B. Zhang, T. Tian, D. Xiao, S. Gao, X. Cai, Y. Lin, Adv. Funct. Mater. 32 (2022) 2109728.
[39] J. Zhang, Y. Xu, C. Zhuo, R. Shi, H. Wang, Z. Hu, H.F. Chan, H.-W. Kim, Y. Tao, M. Li, Biomaterials 294 (2023) 122014.
[40] Y. Jin, H. Wang, K. Yi, S. Lv, H. Hu, M. Li, Y. Tao, Nano-Micro Lett. 13 (2021) 25.
[41] B.T. Tran, J. Kim, D.R. Ahn, Nanoscale 12 (2020) 22945–22951.
[42] H. Hu, H. Gehart, B. Artegiani, L.O.-I. C, F. Dekkers, O. Basak, J. van Es, S.M. Chuva de Sousa Lopes, H. Begthel, J. Korving, M. van den Born, C. Zou, C. Quirk, L. Chiriboga, C.M. Rice, S. Ma, A. Rios, P.J. Peters, Y.P. de Jong, H. Clevers, Cell 175 (2018) 1591–1606.
[43] N. Tanimizu, N. Ichinohe, Y. Sasaki, T. Itoh, R. Sudo, T. Yamaguchi, T. Katsuda, T. Ninomiya, T. Tokino, T. Ochiya, A. Miyajima, T. Mitaka, Nat. Commun. 12 (2021) 3390.
[44] S. Sekiya, A. Suzuki, Nature 475 (2011), 390-U148.
[45] F. Wu, D. Wu, Y. Ren, Y. Huang, B. Feng, N. Zhao, T. Zhang, X. Chen, S. Chen, A. Xu, J. Hepatol. 70 (2019) 1145–1158.
[46] Z. Lu, S.A. Priya Rajan, Q. Song, Y. Zhao, M. Wan, J. Aleman, A. Skardal, C. Bishop, A. Atala, B. Lu, Biomaterials 269 (2021) 120668.
[47] C. Ji, M.L. Qiu, H.T. Ruan, C.D. Li, L. Cheng, J. Wang, C.W. Li, J. Qi, W.G. Cui, L. F. Deng, Adv. Sci. 9 (2022) 1–19.
[48] T. Shinozawa, M. Kimura, Y. Cai, N. Saiki, Y. Yoneyama, R. Ouchi, H. Koike, M. Maezawa, R.R. Zhang, A. Dunn, A. Ferguson, S. Togo, K. Lewis, W.L. Thompson, A. Asai, T. Takebe, Gastroenterology 160 (2021) 831–846 e810.
[49] Y. Kim, Y.W. Kim, S.B. Lee, K. Kang, S. Yoon, D. Choi, S.-H. Park, J. Jeong, Biomaterials 274 (2021) 120899.
[50] I. Sawitza, C. Kordes, S. Götze, D. Herebian, D. Häussinger, Sci. Rep. 5 (2015) 13320.
[51] R. Solhi, M. Lotfinia, R. Gramignoli, M. Najimi, M. Vosough, Trends Endocrinol. Metabol. 32 (2021) 731–745.
[52] S.R. Liu, R.H. Guo, X.L. Hou, Y. Zhang, X.W. Jiang, T.T. Wang, X.Y. Wu, K.Y. Xu, X. P. Pan, L. Qiao, Cytotechnology 72 (2020) 327–341.
[53] X. Liu, X. Wang, L. Zhang, L. Sun, H. Wang, H. Zhao, Z. Zhang, W. Liu, Y. Huang, S. Ji, J. Zhang, K. Li, B. Song, C. Li, H. Zhang, S. Li, S. Wang, X. Zheng, Q. Gu, Adv. Healthcare Mater. 10 (2021) e2101405.
[54] V.L. Dao Thi, X. Wu, R.L. Belote, U. Andreo, C.N. Takacs, J.P. Fernandez, L.A. Vale-Silva, S. Prallet, C.C. Decker, R.M. Fu, B. Qu, K. Uryu, H. Molina, M. Saeed, E. Steinmann, S. Urban, R.R. Singaraja, W.M. Schneider, S.M. Simon, C.M. Rice, Nat. Commun. 11 (2020) 1677.
[55] A. Mardinoglu, R. Agren, C. Kampf, A. Asplund, M. Uhlen, J. Nielsen, Nat. Commun. 5 (2014) 3083.
[56] W.Y. Lai, J.W. Wang, B.T. Huang, E.P.Y. Lin, P.C. Yang, Theranostics 9 (2019) 1741–1751.